



Geochemistry, Geophysics, Geosystems



RESEARCH ARTICLE

10.1029/2021GC009985

Key Points:

- The mantle and core acquired petagrams of helium-3 from the solar nebula
- The core is a major helium-3 reservoir in the Earth
- Helium-3 leaks from the core to the mantle

Correspondence to:

P. L. Olson, peterleeolson@unm.edu

Citation:

Olson, P. L., & Sharp, Z. D. (2022). Primordial helium-3 exchange between Earth's core and mantle. *Geochemistry, Geophysics, Geosystems*, 23, e2021GC009985. https://doi.org/10.1029/2021GC009985

Received 21 JUN 2021 Accepted 14 FEB 2022

Author Contributions:

Conceptualization: Peter L. Olson, Zachary D. Sharp

Formal analysis: Peter L. Olson Funding acquisition: Peter L. Olson, Zachary D. Sharp

Investigation: Peter L. Olson, Zachary D. Sharp

Methodology: Peter L. Olson, Zachary

Project Administration: Peter L. Olson, Zachary D. Sharp

Software: Peter L. Olson Validation: Peter L. Olson

Writing – original draft: Peter L. Olson Writing – review & editing: Peter L. Olson, Zachary D. Sharp

© 2022. The Authors.

This is an open access article under the terms of the Creative Commons Attribution-NonCommercial-NoDerivs License, which permits use and distribution in any medium, provided the original work is properly cited, the use is non-commercial and no modifications or adaptations are made.

Primordial Helium-3 Exchange Between Earth's Core and Mantle

Peter L. Olson¹ and Zachary D. Sharp¹

¹Department of Earth and Planetary Sciences, University of New Mexico, Albuquerque, NM, USA

Abstract Volatiles from the solar nebula are known to be present in Earth's deep mantle. The core also may contain solar nebula-derived volatiles, but in unknown amounts. Here we use calculations of volatile ingassing and degassing to estimate the abundance of primordial ³He now in the core and track the rate of ³He exchange between the core and mantle through Earth history. We apply an ingassing model that includes a silicate magma ocean and an iron-rich proto-core coupled to a nebular atmosphere of solar composition to calculate the amounts of ³He acquired by the mantle and core during accretion and core formation. Using experimentally determined partitioning between core-forming metals and silicate magma, we find that dissolution from the nebular atmosphere deposits one or more petagrams of ³He into the proto-core. Following accretion, ³He exchange depends on the convective history of the coupled core-mantle system. We combine determinations of the present-day surface ³He flux with estimates of the present-day mantle ³He abundance, mantle and core heat fluxes, and our ingassed ³He abundances in a convective degassing model. According to this model, the mantle ³He abundance is evolving toward a statistical steady state, in which surface losses are compensated by enrichments from the core.

Plain Language Summary Each year, about 2 kg of the rare gas helium-3 escapes from Earth's interior, mostly along the mid-ocean ridge system. Helium-3 is primordial, created shortly after the Big Bang and acquired from the solar nebula as the Earth formed. Geochemical evidence indicates the Earth has deep reservoirs of helium-3, but their locations and abundances remain uncertain. Our models of volatile exchange during Earth's formation and evolution implicate the metallic core as a leaky reservoir that supplies the rest of the Earth with helium-3. Our results also suggest that other volatiles may be leaking from the core into the mantle.

1. Introduction

Earth's inventory of helium consists of two stable isotopes, the more abundant ⁴He and the far more rare ³He. Unlike terrestrial ⁴He, which is mainly produced by decay of uranium and thorium, terrestrial ³He is largely of primordial origin, synthesized in the aftermath of the Big Bang (Bania et al., 2002) and incorporated into the Earth primarily during its formation (Lupton & Craig, 1975). In spite of its primordial status and 4.56 Gy of planet evolution, ³He continues to leak from Earth's interior.

Much attention has been given to 3 He in ocean island basalts (OIBs), particularly those with high 3 He/ 4 He ratios that indicate a deep source region with less volatile loss than the upper mantle (Mukhopadhyay & Pari, 2019). But on a global scale, transport of 3 He associated with OIB is relatively minor in comparison to the larger transport out of the mantle that occurs in major ocean basins and results from ocean crust production at spreading centers. The present-day mid-ocean ridge basalt (MORB) 3 He flux amounts to 527 ± 102 mol/y globally (Bianchi et al., 2010) and is concentrated at active spreading centers (Lupton et al., 1977). 3 He flux also occurs at island arcs (Poreda & Craig, 1989), in continental extension zones (Torgersen, 1993), as well as volcanic hot spots (Kurz et al., 1982), although the sum of these is probably less than 20% of the MORB flux (see Section 5).

The surface flux of ³He is useful for calibrating the flux of other volatiles from the mantle, and also provides constraints on the origin and abundance of noble gases, as well as the degassing history of the Earth's interior. Its global distribution, along with its connections to magmatic and hydrothermal activity tied to plate tectonics, implies that much of the observed ³He flux results from upward transport of helium by the general convective circulation of the mantle. What is not clear is where in Earth's interior the ³He that supplies that flux originated, and where it now resides.

OLSON AND SHARP 1 of 18

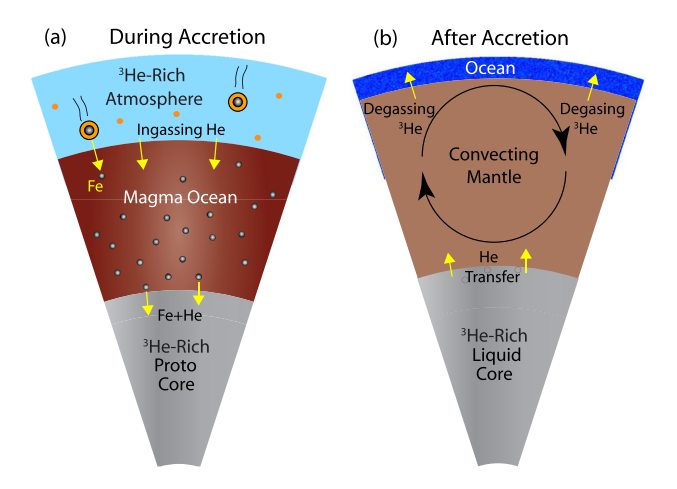


Figure 1. Sketches illustrating core-mantle helium exchange processes.

(a) ³He acquisition during Earth's accretion by ingassing from the nebular atmosphere and transport through the magma ocean to the proto-core, and (b) ³He transport from the core to the mantle and from the mantle to the ocean after accretion.

A major challenge for retaining primordial ³He in the early mantle is preservation in the face of enhanced atmospheric escape (Erkaev et al., 2013; Hunten et al., 1987; Kuramoto et al., 2013; Lammer et al., 2014) and atmosphere loss during giant impacts (Melosh & Vickery, 1989; Sakuraba et al., 2019; Schlichting & Mukhopadhyay, 2018), particularly impacts that produce extensive melting and vapourization (Carter et al., 2020) such as the Moon-forming event (Canup, 2012; Cuk & Stewart, 2012; Nakajima & Stevenson, 2015; Porcelli & Halliday, 2001). Degassing during magma ocean solidification (Elkins-Tanton, 2012; Pahlevan & Stevenson, 2007; Solomatov, 2007) plus later degassing from multiple cycles of plate tectonics and mantle convective overturn (Pepin & Porcelli, 2006; Van Keken & Ballentine, 1998; Van Keken et al., 2001) add to the loss. Once removed from the interior, little helium is recycled back into the mantle (Dygert et al., 2018) and it readily escapes from the Earth system (Lammer et al., 2008), so that deep-seated ³He is not replenished.

The core offers a possible reservoir for ³He because it is less vulnerable to large impacts compared to other parts of the Earth system, it does not participate directly in plate cycling, and it has remained mostly liquid over Earth's history. It has often been proposed that hydrogen, helium and other noble gases may reside in the core (Jephcoat, 1998; Porcelli & Halliday, 2001; Wu et al., 2018; Zhang & Yin, 2012), but questions about partitioning of vola-

tiles between core metals and silicate melts and the amount of metal-silicate equilibration during core formation had prevented definitive answers. Now, however, diamond cell experiments have measured helium partitioning between silicate liquids and iron liquids up to 16 GPa (Bouhifd et al., 2013), and between solid silicates and liquid iron alloys at 1 GPa (Roth et al., 2019), isotope studies indicate substantial metal-silicate equilibration occurred during core formation (Kleine & Rudge, 2011; Kleine & Walker, 2017), and noble gas isotopes from the solar nebula with Earth-like ratios have been found in iron meteorites (Vogt et al., 2021).

Although there is less unanimity on ³He partitioning at lower mantle pressures and temperatures (Matsuda et al., 1993; Wang et al., 2022), it seems increasingly likely that ³He *could* have been deposited in the core. Key remaining questions concern *amounts*: How much ³He did the core acquire as it formed, and since that time, how much has it surrendered to the mantle? In this paper we use models of volatile ingassing and degassing that yield quantitative estimates of the amount of ³He now in the core and the rates of ³He exchange between the core and mantle through Earth history. We focus on two distinct exchange processes: ³He ingassing during Earth's accretion and later ³He degassing driven by mantle convection.

2. Core-Mantle ³He Exchange

The sketches in Figure 1 illustrate two processes in the evolution of Earth's ³He budget that are examined in this study. Early in its accretion the proto-Earth was enveloped in solar nebula gas. Terrestrial planet formation theory and models indicate that if the proto-Earth grew to 0.3 or more of its final mass within the solar nebula, it would have attracted a dense hydrogen and helium-rich atmosphere (Sasaki, 1999) capable of supporting a high-temperature silicate magma ocean (Ikoma & Genda, 2006) above the molten proto-core, as illustrated in Figure 1a. In such an environment, accreting pebbles and planetesimals (Johansen et al., 2021; Levison et al., 2015; Nimmo et al., 2018) supply iron-rich compounds to the magma ocean, while dynamical processes near the magma ocean surface dissolve helium from the high-pressure atmosphere (Mizuno et al., 1980; Olson & Sharp, 2018; Sharp, 2017). Experiments indicate that a only small fraction of the helium dissolved in the silicate liquid partitions into the iron-rich liquids as they sink through the magma ocean, yet this is enough to deliver abundant ³He to the proto-core.

The cataclysmic events listed in the Introduction are expected to have depleted the mantle of dissolved volatiles relative to the core. Giant impacts in particular may have played an important role in early Earth's helium budget. According to calculations of atmosphere evolution following giant impacts, nearly complete loss the nebular atmosphere is expected if the impactor mass exceeds 5% of Earth's mass (Biersteker & Schlichting, 2021). This

OLSON AND SHARP 2 of 18



implies that a Moon-forming impact with the embryo Theia less than half the size of Mars could remove essentially all of the helium in the atmosphere. And if that atmosphere removal mechanism consisted of a Parker wind driven by impact heat deposited in the interior, it would likely have continued to expel helium from the Earth system for millions of years following the impact.

The amount of helium lost from the interior during this time is difficult to estimate because it depends sensitively on how the magma ocean solidified. As silicate magma begins to crystallize, volatiles are excluded from the solid phase and become strongly enriched in the residual liquid. Accordingly, if a magma ocean solidifies in the upward direction, as is generally expected (Solomatov, 2007), volatiles become progressively concentrated above the melt-solid interface (Elkins-Tanton, 2012). Near the magma ocean surface, the volatile-enriched melt saturates and gas bubbles nucleate. Bubbles formed this way add buoyancy to parcels of magma, propelling the parcels closer to the surface, whereupon the bubbles release their volatiles into the atmosphere (Elkins-Tanton, 2011). At the same time, turbulent atmospheric winds disturb the magma surface (Olson & Sharp, 2019), creating a localized environment for additional helium degassing. In short, the combination of gradual upward magma ocean solidification coupled with surface mixing is capable of extracting a very large fraction of the ³He from the early mantle. Nevertheless, volatile expulsion by upward crystallization is not completely efficient. Some amount of ³He is retained in the mantle wherever gas-rich melt becomes trapped interstitially in the crystallizing magma.

Assuming that the early mantle was strongly depleted in helium by these processes, a disequilibrium in chemical potential would exist across the core-mantle boundary (CMB), such that ³He would leak from the core back into the mantle over geologic time. Figure 1b illustrates the control on this leakage by subsolidus mantle convection. Helium leaks across the CMB in response to the difference in chemical potential there; it then diffuses into the lower mantle, similar to the diffusive core-to-mantle heat flux. Much of the ³He leaving the core is then carried toward the surface within the general convective circulation of the mantle, where it is diluted with ⁴He prior to its surface release, mostly into the ocean via MORB formation. In addition, it is possible that some of the ³He leaving the core is sequestered for a time in the deep mantle and later transported upward within localized mantle plumes and released via OIB formation.

The helium exchange processes illustrated in Figures 1a and 1b require separate model treatments, for several reasons. First, they apply at different points in Earth history, operate on vastly different timescales, and involve different physical and chemical conditions. Second, our model assumes that nebular ingassing and subsolidus convective degassing were separated in time by the late-accretion volatile loss mechanisms just described. In spite of their importance to Earth's helium budget, modeling these late-accretion events is beyond the scope of this study. Instead, we adopt a before-and-after approach. We first model the nebular ingassing process (Figure 1a), which yields estimates of the amount of nebular ³He originally deposited in the mantle and core. We then model Earth's convective degassing history (Figure 1b) starting from the present-day and working backward in time, which yields estimates for the post-accretion ³He abundances in the mantle and core. Comparing the post-accretion mantle abundance with the ingassed abundance provides an estimate of ³He lost from the mantle during late accretion. Equating the post-accretion core abundance to the ingassed abundance provides an estimate of the ³He now in the core, as well as the amount of ³He now in the mantle that was originally deposited in the core.

3. Ingassing Model

Our model for nebular ingassing during proto-Earth accretion consists of one-dimensional growing mantle and core coupled to a one-dimensional atmosphere of solar composition, the atmosphere, core, and mantle all derived from solar nebula gas and solids. This model formulation adheres to that in Olson and Sharp (2018) and Olson and Sharp (2019) in most particulars. Aspects of our ingassing model that are identical to those in Olson and Sharp (2019) are summarized below but not described in detail. Instead, only the new aspects of this model are described in detail in this Section. The full set of model physical properties are given in Tables 1 and 2.

Accretion of the proto-Earth is represented by a continuous mass addition phase followed later by a discrete mass addition representing the Moon-forming event. We use an exponential accretion rate during the continuous phase, as specified below. We assume the accretion adds mass with the same core-forming metal mass fraction as the proto-Earth, and that metal-silicate segregation and partial metal-silicate equilibrium proceed in step with accretion, with silicates and oxides added to the mantle and metals to the proto-core. Only mean values are used

OLSON AND SHARP 3 of 18



Ingassing Model Properties Property	Notation	Value(s)
<u> </u>		
Earth mass, present	M_E	$5.97 \times 10^{24} \mathrm{kg}$
Mantle, core mass, present	M_m, M_c	$4.0, 1.94 \times 10^{24} \mathrm{kg}$
Proto-Earth mass, accreted	M_p	$5.37 \times 10^{24} \mathrm{kg}$
Core mass fraction	M	0.325 kg/kg
Mantle density, mean	$ ho_m$	$4 \times 10^3 \mathrm{kg/m^3}$
Core density, mean	$ ho_c$	$10 \times 10^3 \mathrm{kg/m^3}$
Accretion time scale	t_p	4–25 My
Solar nebula lifetime	t_d	4 My
Solar UV flux	q_{ph}	$10.5 \times 10^{-2} \mathrm{W/m^2}$
Accretion heat distribution	γ	0.01
Heat density, decay time, ²⁶ Al	H_{Al},t_{Al}	$1.9 \times 10^{-7} \text{ W/Kg}, 1.05 \text{ My}$
Atmosphere bulk composition	H ₂ , He	0.85, 0.15 mol/mol
Atmosphere helium ratio	³ He/ ⁴ He	1.5×10^{-4}
Atmosphere opacity	σ	$3.5 \times 10^{-4} \text{ m}^2/\text{kg}$
Atmosphere gas constant	R'	$3.6 \times 10^3 \text{ J/kg/K}$
Atmosphere escape efficiency	β	0.15-0.75
Atmosphere wind speed	U	1–10 m/s
Nebula, photosphere temperature	T_{neb},T_{ph}	280, 400 K
Magma $P = 0$ solidus, liquidus	T_{ms0} , T_{ml0}	1425, 2000 K
Magma melting coefficients	a_{ms}, a_{ml}	24, 28 K/GPa
Magma rheological temperature	T_{l}	1700 K
Magma kinematic viscosity	$ u_m$	$2 \times 10^{-4} \text{ m}^2/\text{s}$
Magma specific heat	C_m	$1 \times 10^3 \text{ J/kg/K}$
Magma thermal expansion coefficient	$lpha_{ml}$	$5 \times 10^{-5} / \text{K}$
Magma He diffusivity	$\kappa_{ m He}$	$5 \times 10^{-9} \mathrm{m}^2/\mathrm{s}$
Mantle He diffusivity, CMB	$\kappa_{ m He}$	$1 \times 10^{-10} \mathrm{m}^2/\mathrm{s}$
Mantle thermal expansion coefficient	$lpha_{ms}$	3×10^{-5} /K
Magma Solubility, ³ He	$K_{ m He3}$	1.1×10^{-3} kg/kg/GPa
Magma thermal diffusivity	K_m	$1 \times 10^{-6} \mathrm{m}^2/\mathrm{s}$
Core $P = 0$ liquidus	T_{cl0}	1800 K
Core melting coefficients	a_{c1}, a_{c2}	20 K/GPa, -0.025 K/GPa ²
Core specific heat	c_c	$0.85 \times 10^3 \text{J/kg/K}$
Core thermal expansion coefficient	$lpha_c$	1.5×10^{-5} /K
Core pressure, reference	P_{ref}	130 GPa
Metal-silicate equilibrium	k	0.25-1.0
Metal-silicate ³ He partition	D_{ll}	0.01

Note. Subscripts: p, m, c, s = proto-Earth, mantle (magma), core, atmosphere, surface; d, l, E = nebula dissipation, liquid, Earth. He, ref = helium, reference. cmb, ph, Al = core-mantle boundary, photosphere, 26 Al.

for the density of the mantle and core, respectively, with the effects of compressibility limited to calculations of the temperature profiles and melting curves.

We adopt an exponential accretion history with the following form, similar to that used to infer Earth formation timescales from isotopic data (Kleine & Rudge, 2011):

OLSON AND SHARP 4 of 18



Table 2 Degassing Model Properties		
Property	Notation	Value
Mantle, core masses, present-day	M_m, M_c	$4.0, 1.94 \times 10^{24} \text{ kg}$
³ He surface flux, present-day	$F_s(0)$	1.8 kg/y
³ He mantle abundance, present-day	$M_{m}C_{m}\left(0\right)$	10, 30, 100 Tg
³ He diffusivity, lower mantle	κ_{He}	$1 \times 10^{-10} \text{ m}^2/\text{s}$
Thermal diffusivity, lower mantle	κ_T	$1 \times 10^{-6} \mathrm{m}^2/\mathrm{s}$
Specific heat, mantle	C_m	1200 J/kg-K
Metal-silicate ³ He partition, CMB	D_{ls}	1, 10 kg/kg
Ocean crust ³ He enrichment	e_{He}	10
Mantle heat flux, 0-4.4 Ga	$Q_{\scriptscriptstyle m}$	32-64 TW
Core (CMB) heat flux	$Q_{ m cmb}$	13 TW
CMB thermal boundary layer	$\Delta T_{ m cmb}$	1200 K
Mantle potential temperature	T_{mp}	1600 K

Note. Subscripts: m, c, mp, He, T = mantle, core, mantle potential, helium, thermal. s, cmb, ls = surface, core-mantle boundary, liquid-solid.

$$M(t) = M_p \left(1 - \exp\left(-\frac{t}{t_p}\right) \right) \tag{1}$$

where M is the proto-Earth mass, M_p is the proto-Earth mass at the end of continuous accretion and prior to Moon formation, t is time during accretion, and t_p is the accretion timescale. The proto-Earth mass consists of proto-mantle and proto-core parts denoted by subscripts m and c, such that $M = M_m + M_c$. We assume constant core-forming metal fraction during accretion, such that $M_c = \mu M$ at all times, with $\mu = 0.325$.

Accretion energetics involve a balance between energy inputs and losses. Ranked according to the amount of energy delivered, the inputs we consider are: accretion energy (kinetic energy of impacts), energy release through segregation of core metals, radioactive heating (primarily from ²⁶Al decay) and sensible heat content of the impactors, hereafter referred to as planetesimal heat. Energy losses are represented by surface luminosity, equal to the total surface heat flux; energy transfers within the interior include sensible heating and cooling, melting and solidification, and core-mantle heat exchange. The temperature structure of the proto-Earth and its nebular atmosphere are assumed to be in statistical equilibrium with these energy sources at all times.

3.1. Nebular Atmosphere

The nebular atmosphere history in our ingassing model includes a growth phase in which gas is captured gravitationally from the solar nebula, followed by an erosion phase after the solar nebula dissipates. Following Olson and Sharp (2019), we assume hydrostatic force balance and a radiative thermal balance with uniform opacity $\sigma = 3.5 \times 10^{-4}$ m²/kg for the basic state of the atmosphere, with the photosphere marking top of the radiative layer defined by an isotherm. The small value of opacity used here is predicated on the assumption that the magma ocean acts as an efficient sink of atmosphere dust. The atmosphere gas composition is approximately solar and consists of a (0.85, 0.15) hydrogen-helium mixture with 3 He/ 4 He = 1.5 × 10 $^{-4}$. Atmospheric wind, the driver for gas transfer to the interior, is based on the energy balance described above, and the proto-Earth rotation rate is taken to be twice the present-day rotation rate.

The nebular atmosphere in its growth phase has the following radial structure (Sasaki & Nakazawa, 1990):

$$T_{a} = \frac{GM}{4R'} \frac{1}{r} + T_{neb}; \quad P_{a} = \frac{16\pi k_{B}GMT_{a}^{4}}{3\sigma L_{s}}; \quad \rho_{a} = \frac{16\pi k_{B}GMT_{a}^{3}}{3R'\sigma L_{s}}$$
(2)

where T_a , σ , and L_s are atmosphere temperature, opacity, and surface luminosity, respectively, k_B is the Stefan-Boltzmann constant, P_a is atmosphere pressure, ρ_a is atmosphere density, G is the gravitational constant, r is radial distance, T_{neb} is the local nebula temperature, and R' is the modified gas constant. The surface luminosity (total surface heat flow, denoted by subscript s) is given by $L_s = \sum L_i$ with

$$L_1 = \frac{GM}{r_s} \frac{dM}{dt}; \quad L_2 = \mu \left(\frac{\rho_c - \rho_m}{\rho_c}\right) (g_s r_s - g_{cmb} r_{cmb}) \frac{dM}{dt} \quad L_3 = \bar{c} T_{neb} \frac{dM}{dt}$$
(3)

and

$$L_4 = H_{AI} M_m e^{-t/t_{AI}}; \quad L_5 = -c_m \frac{d\overline{M_m T_m}}{dt} - c_c \frac{d\overline{M_c T_c}}{dt}; \quad L_6 = -h_m \frac{d\overline{M_m f_{melt}}}{dt} - h_c \frac{d\overline{M_c f_c}}{dt}$$
(4)

where r_s and r_{cmb} are surface and proto-core-mantle boundary radii, g_s and g_{cmb} are gravity there, \overline{T}_m , \overline{T}_c , ρ_m , ρ_c and \overline{f}_{melt} , \overline{f}_c are proto-mantle and proto-core mean temperatures, densities and melt fractions, respectively, c_m , c_c and h_m , h_c are their specific and latent heats, \overline{c} is the proto-planet average specific heat, and H_{Al} and t_{Al} are the densities and decay times for 26 Al, respectively. In Equation 3, L_1 represents heat from the kinetic energy of impacts (assumed to be dissipated in the proto-Earth interior or on its surface), L_2 represents heat from segregation of core

OLSON AND SHARP 5 of 18



metals, L_3 represents planetesimal heat, L_4 represents radioactive heating, L_5 represents sensible heating, and L_6 represents latent heating.

Erosion of the nebular atmosphere is assumed to occur via energy-limited hydrodynamic escape, driven by the short wavelength energy flux from the early Sun. The atmosphere mass loss rate is given by

$$\frac{dM_a}{dt} = -\frac{\pi \beta r_{ph}^3 q_{ph}}{GM},\tag{5}$$

where M_a is the atmosphere mass below the photosphere radius r_{ph} (taken to coincide with the exobase), q_{ph} is the short wavelength solar radiative flux at the proto-Earth orbital distance driving hydrodynamic escape, and β is the hydrodynamic escape efficiency factor (Erkaev et al., 2016; Genda & Ikoma, 2008). We write q_{ph} as the sum of extreme ultraviolet (denoted by subscript EUV) and Lyman- α contributions:

$$q_{ph} = q_{EUV} + q_{\alpha}. \tag{6}$$

Following Genda and Ikoma (2008), we use constant values of $q_{EUV} = 0.08 \text{ W/m}^2$ and $q_{\alpha} = 0.025 \text{ W/m}^2$ for times t less than 100 My, corresponding to a combined flux approximately 50 times greater than today. For the photosphere radius, we specify the temperature there, $T_{ph} = 400 \text{ K}$. In terms of the surface temperature T_s and surface radius r_s , the photosphere radius is then

$$r_{ph} = \left(\frac{T_s}{T_{ph}}\right) r_s. \tag{7}$$

The surface pressure, temperature, and density during atmosphere erosion are given by

$$P_{s} = \frac{GMM_{a}}{16\pi r_{s}^{4} \ln(r_{ph}/r_{s})}; \quad T_{s} = \left(\frac{3\sigma L_{s} P_{s}}{16\pi k_{B} GM}\right)^{1/4}; \quad \rho_{s} = \frac{P_{s}}{R' T_{s}}$$
(8)

The peak surface temperature and the peak surface pressure occur simultaneously near the end of the solar nebula, at time t_d , the transition between atmosphere growth and erosion. According to the formulas above, these are given by

$$T_{s}(t_{d}) = \frac{GM(t_{d})}{4R'r_{s}(t_{d})} + T_{neb}; \quad P_{s}(t_{d}) = \frac{16\pi k_{B}GM(t_{d})}{3\sigma L_{s}(t_{d})} T_{s}(t_{d})^{4}. \tag{9}$$

Based on the numerical values for the model input parameters given in Table 1, peak surface temperatures and pressures from Equation 9 are in the ranges 2000–2400 K and 200–300 bar, respectively.

3.2. Proto-Earth Interior

The internal thermal structure of our model proto-Earth consists of adiabatic temperature profiles in the proto-mantle and core interiors at all times when impact heating plus the heat generated by segregation of core-forming metal exceeds secular cooling. We specify a rheological transition temperature for the mantle $T_l = 1700$ K, above which the mantle surface behaves like a low viscosity liquid in terms of its dynamics, that is, behaves like a global surface magma ocean, hereafter abbreviated GSMO. When the temperature at base of the atmosphere T is above T_l , the potential temperature of the mantle matches T_s . When T_s is below T_l we add a temperature jump between the atmosphere base and the mantle potential temperature. This temperature jump represents the thermal effect of a thin mantle lid, effectively a partially or totally solidified crust across which the temperature increases rapidly from T_s to T_l .

Adiabatic temperature gradients in the proto-mantle and proto-core are given by

$$\frac{d\ln(T_m)}{dr} = -\frac{\alpha_m g_m}{c_m}; \quad \frac{d\ln(T_c)}{dr} = -\frac{\alpha_c g_c}{c_c}$$
 (10)

where T_m , T_c , α_m , α_c , g_m , g_c are mantle and core adiabatic temperature, thermal expansivity, and gravity profiles. Melt fractions in the interior are calculated by comparing the adiabats in the proto-mantle and proto-core to pressure-dependent laws for the mantle solidus and liquidus and for core melting. Proto-mantle melting is based

OLSON AND SHARP 6 of 18



on deKoker and Stixrude (2009). We prescribe the mantle (magma) solidus temperature T_{ms} and liquidus temperature T_{ml} to vary linearly with mantle hydrostatic pressure P_m according to

$$T_{ms} = T_{ms0} + a_{ms}P_m \tag{11}$$

and

$$T_{ml} = T_{ml0} + a_{ml} P_m (12)$$

with T_{ms0} , T_{ml0} , a_{ms} , and a_{ml} given in Table 1. We assume the proto-mantle melt fraction f_{melt} varies linearly between the magma solidus and liquidus.

In calculating the adiabatic temperature variation in the proto-mantle, we apply different values of the thermal expansion coefficient depending on whether the material is solid or contains melt. In solid regions (where $f_{\text{melt}} = 0$) we use a smaller constant thermal expansion coefficient α_{ms} , and where liquid magma is present (where $f_{\text{melt}} > 0$) we use a larger (but still constant) thermal expansion coefficient α_{ml} in order to account for phase changes (Solomatov, 2007). For the values of α_{ms} and α_{ml} given in Table 1, typical adiabats in the magma lie nearly parallel to the curves of constant melt fraction f_{melt} , whereas the adiabats in solid regions of the proto-mantle are less steep.

Core melting is based on Anzellini et al. (2013). We use a quadratic formula for the liquidus in terms of core hydrostatic pressure P_c , with the form

$$T_{cl} = T_{cl0} + a_{c1}P_c + a_{c2}P_c^2 (13)$$

with T_{cl0} and the coefficients a_{c1} and a_{c2} also given in Table 1.

We calculate ΔT_{lid} , the temperature jump across the lid (applied only when the atmosphere surface temperature falls below T_i) as

$$\Delta T_{lid} = \frac{\gamma L_s}{\rho_m c_m A_s} \left(\frac{dr_s}{dt}\right)^{-1} \tag{14}$$

where ρ_m , c_m , and A_s are proto-mantle density, specific heat and surface area, respectively, dr_s/dt is the rate of increase of the surface radius, and γ is the heat distribution coefficient measuring the fraction of the accretion energy deposited as heat in the lid. Our calculations use $\gamma = 0.01$.

3.3. Helium Exchange

Gas exchange between the atmosphere and interior is allowed only during GSMO times. We enforce chemical equilibrium between the atmosphere and magma at the magma surface, but not in the mantle interior. Similarly, we enforce chemical equilibrium between the proto-core and mantle at the CMB but not throughout the interior of either region. Solubility of helium in the magma is based on Henry's law. Helium fluxes between atmosphere and GSMO are calculated three ways: (a) assuming the impactors are equilibrated with the atmosphere at its base (Ikoma & Genda, 2006); (b) diffusion based on the magma surface age (Olson & Sharp, 2018), and (c) using a model of wind mixing derived from air-sea interaction studies (Olson & Sharp, 2019). These methods yield somewhat different volatile abundances, but within a factor of three of each other according to our testing, which is not enough difference to affect our qualitative conclusions. The results shown in the next section are based on wind mixing, for which the surface 3 He flux F_{s} is given by

$$F_s = -\epsilon \rho_s \left(\frac{\kappa_{He}}{\nu_m}\right)^{1/2} A_s \left(C_s - C_m\right) U, \tag{15}$$

where ρ_s is the atmosphere surface density, $\kappa_{\rm He}$ and ν_m are helium diffusivity and kinematic viscosity in the magma, U is near-surface wind speed, C_m and C_s are the average magma 3 He concentrations in its interior and at its surface, $\epsilon \simeq 0.01$, and the negative sign denotes downward flux, from the atmosphere into the magma. In Equation 15, $C_s = K_{\rm He3} P_{\rm He3}$ where $P_{\rm He3}$ and $K_{\rm He3}$ denote the 3 He partial pressure and Henry's law solubility coefficient in magma, respectively.

OLSON AND SHARP 7 of 18

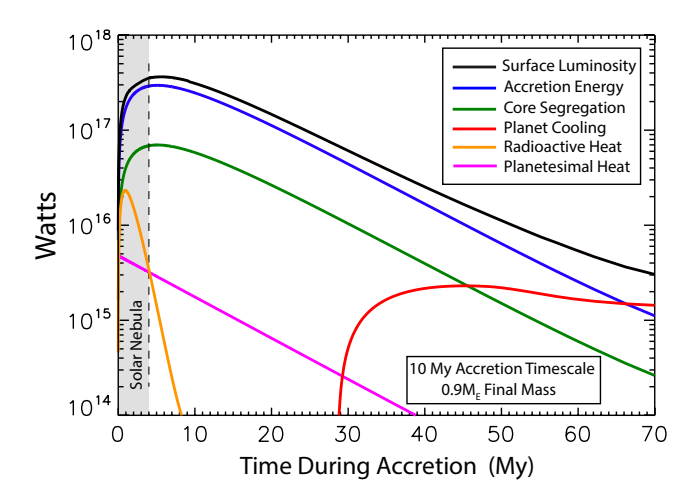


Figure 2. Energy inputs during proto-Earth accretion in terms of Watts of power versus time. The case shown here is for the solar nebula lasting 4 My (shading), continuous accretion to $0.9M_E$ with a 10 My exponential timescale, and atmosphere escape efficiency 0.15. Surface luminosity is the sum of the other five energies.

Helium transport from the magma ocean to the proto-core is assumed to occur via a two-step process. First, partial ³He equilibrium between core-forming metals and silicate melts is established in the magma ocean; second, these helium-bearing metals segregate into the proto-core. We require that both of these steps keep pace with accretion, so that the metal abundance in the magma ocean remains small at all times. The flux of ³He across the CMB during accretion is then proportional to the core growth rate and is given by

$$F_{cmb} = -kD_{ll}C_m\mu\frac{dM}{dt},\tag{16}$$

where D_{ll} is the liquid metal-liquid silicate partition coefficient for helium, k is the fraction of the metal that equilibrates with the silicates in the magma ocean during accretion, $\mu dM/dt$ is the accretion rate of the proto-core, and the negative sign again denotes downward flux. Small corrections to (16) for situations where the magma melt fraction $f_{\rm melt} < 1$ are ignored here. For ³He partitioning in the magma ocean we use $D_{ll} = 0.01$ (Bouhifd et al., 2013), independent of pressure and temperature. For the metal-silicate equilibration factor k, interpretations of isotope data commonly involve a tradeoff between k in Equation 16 and the accretion timescale t_p (Kleine & Rudge, 2011). Based on Figure 7 in Kleine and Walker (2017), we parameterize this tradeoff over the range 4 My $< t_p < 25$ My as $k = 2/\sqrt{t_p}$.

4. Ingassing Results

Figure 2 shows the time variations of the energy inputs during proto-Earth growth expressed as Watts of power, from an accretion calculation in which the solar nebula lasts $t_d = 4$ My, continuous accretion to $M_p = 0.9 M_E$ on an exponential accretion timescale of $t_p = 10$ My, and hydrodynamic escape efficiency $\beta = 0.15$. This case was

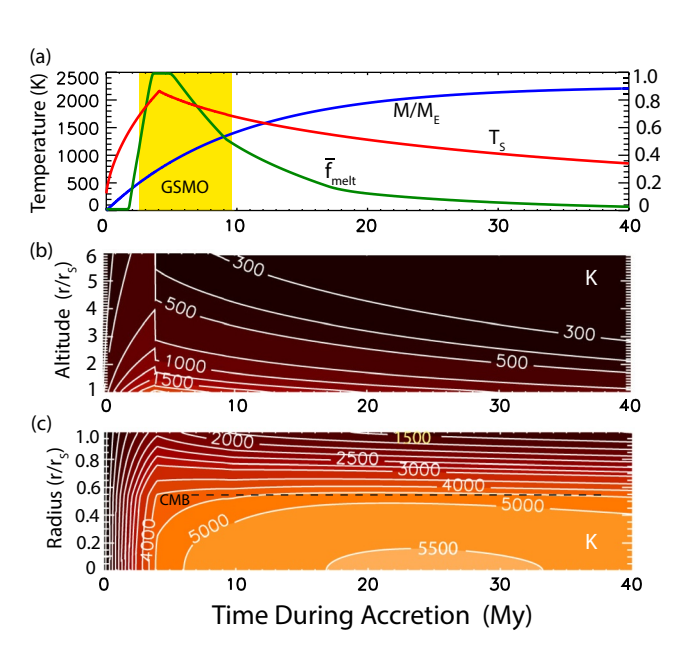


Figure 3. Atmosphere and proto-Earth interior evolution for the energy inputs shown in Figure 2. (a): Proto-Earth accretion history (mass M relative to Earth mass M_E), surface temperature T_s and proto-mantle average melt fraction \bar{f}_{melt} . Global surface magma ocean (GSMO; shading) corresponds to surface temperatures above the silicate rheological transition temperature of 1700 K. (b): Temperature profile in the atmosphere. (c): Temperature profile in the proto-mantle and proto-core. The boundary between the proto-core and protomantle is labeled core-mantle boundary and is indicated by the dashed line.

chosen for illustration because (a) the 4 My solar nebula lifetime approximately corresponds to the youngest chondrule ages (Villeneuve et al., 2009); (b) the 10 My accretion timescale is characteristic of terrestrial protoplanet formation by pebble accretion (Johansen et al., 2021; Lambrechts & Johansen, 2012; Levison et al., 2015) or by accretion starting from an annular distribution of planetesimals (Hansen, 2009); (c) the accretion timescale implies a metal-silicate equilibrium factor k = 0.63, consistent with Hf-W and U-Pb isotopic constraints on core formation (Kleine & Walker, 2017; Nimmo et al., 2018), and (d) it allows for a late $0.1M_E$ addition by the Moon-forming event (Canup, 2012; Cuk & Stewart, 2012).

According to Figure 2, the surface luminosity peaks a few million years after solar nebula dissipation, decreasing thereafter on the accretion timescale. Proto-Earth cooling (sensible heat loss) transitions from negative to positive around 30 My after accretion begins, exceeding in magnitude the main energy inputs after about 65 My. This energy transition serves as a marker for the time when the proto-Earth transitioned from an accretion-dominated regime to one dominated by secular cooling. In rough terms, this transition (beginning at 30 My) also marks the limit of validity of the assumptions that underlie our accretion model. However, as demonstrated below, volatile acquisition by ingassing and volatile partitioning between the magma and proto-core are essentially complete before this transition occurs.

In Figure 3a we compare the evolution of proto-Earth mass, surface temperature and proto-mantle (magma) melt fraction from t=0 to 40 My for the same 10 My accretion timescale, 4 My solar nebula lifetime, and the other parameters used in Figure 2. Shading in the top panel indicates the time interval during which a GSMO is maintained, that is, the time interval when the

OLSON AND SHARP 8 of 18

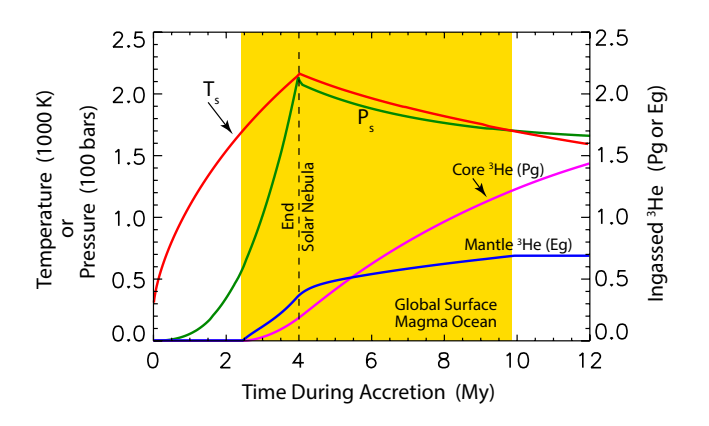


Figure 4. Evolution of surface and interior variables in detail, spanning the first 12 My of Figure 3. Shown are surface temperature T_s , surface pressure P_s , and the proto-mantle and proto-core 3 He abundances in exagrams (Eg = 10^{18} g) and petagrams (Pg = 10^{15} g), respectively. The global surface magma ocean is indicated by shading; the end of the solar nebula is marked by the dashed line.

surface temperature exceeds the rheological transition temperature T_l , allowing ingassing to occur. The curve labeled \bar{f}_{melt} in Figure 3a is the volume average of the melt fraction in the magma. The radial distribution of magma melt is not properly represented in our model because we do not allow for relative motion between the solid and liquid silicate phases (i.e., phase separation or compaction). Although complete proto-Earth melting lasts for less than 2 million years, the proto-mantle contains at least 50% melt through the duration of the GSMO and at least 20% melt until 16 My, implying that the dissolved helium has ample time and access to both components for partitioning between the liquid metal and the silicate magma.

Figures 3b and 3c show the evolution of temperature in the atmosphere and in the interior, respectively. The kinks in temperature near 4 My in these figures correspond to the time of evaporation of the solar nebula, when the temperature at the top of the atmosphere drops from its nebular value (280 K) to the interplanetary value (5 K). The horizontal dashed line labeled CMB in the interior temperature (lower panel) marks the relative depth of the CMB. As the proto-Earth mass increases, the CMB temperature exceeds 4000 K, implying that the proto-core was entirely molten within a few million years. Starting around 18 My, the proto-core begins to cool overall, as the rate of accretion and the surface temperature begin to fall. Yet the CMB temperature

remains above 4500 K until about 35 My, indicating the proto-core remains molten from the onset of the GSMO through the end time of the model validity.

Figure 4 shows the variation of surface temperature, surface pressure, and ³He acquired by the proto-mantle and core during the first 12 My of the calculation in Figure 3. The surface temperature peaks at 2165 K and the surface pressure peaks at 215 bars at approximately the time the solar nebula dissipates, as dictated by Equation 9. Although the GSMO persists for less than 7.5 My in this calculation, the surface pressure is high enough and the atmospheric winds are strong enough (1–10 m/s) to dissolve about 690 Pg (0.69 Eg) of ³He into the magma. Of this amount, approximately 2.2 Pg is ultimately transported into the proto-core, with 1.2 Pg transported during GSMO time. Note that mantle-to-core transport of ³He continues past GSMO times, as long as accretion continues to add core-forming metals and a substantial fraction of the proto-mantle remains molten.

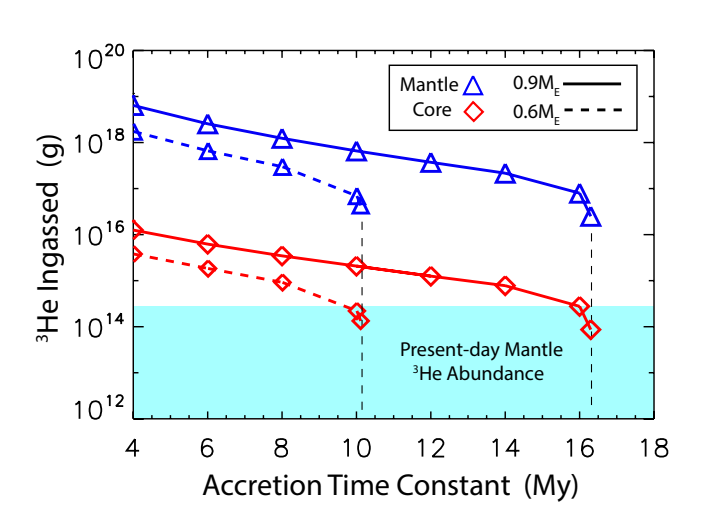


Figure 5. Proto-mantle and proto-core ³He abundances acquired by ingassing versus accretion time constant, for final accreted masses equal to 0.9 and 0.6 of Earth's mass, respectively, and a 4 My nebula lifetime. Shading indicates the estimated range of present-day mantle ³He abundance. Vertical dashed lines mark limiting accretion time constants for ingassing.

Figure 5 shows the amounts of ³He acquired by the mantle and core by nebular ingassing as a function of the accretion time constant t_p , for two different final masses, $M_p = 0.9 M_E$ and $0.6 M_E$, all other parameters the same as in Figures 2–4. The range of ³He abundances estimated for the present-day mantle (explained in the next section) is indicated by shading. The vertical dashed lines mark the limit of ingassing for each final mass, beyond which our model fails to sustain a GSMO. These limits approximately correspond to the ratio $t^* = t_d Mp/t_p M_E \simeq 0.24$. In all cases where ingassing occurs, that is for $t^* < 0.24$, the calculated core ³He abundances equal or exceed present-day mantle abundance estimates, and the calculated mantle 3He abundances far exceed them. Satisfying the above inequality requires relatively fast accretion and a relatively long-lived solar nebula. Nevertheless, they lie within the limits inferred from mantle isotopes (Kleine & Walker, 2017), iron isotopes from meteorites (Schiller et al., 2020), and are also consistent with predictions from pebble accretion (Johansen et al., 2021) as well as some large-impact accretion models (Hansen, 2009; Walsh & Levison, 2016).

In addition to t^* , the results in Figure 5 depends on a large number of the model parameters listed in Table 1. However, most of these dependencies are weak, in that modest changes to their values have only minor effects on the ingassed 3 He abundances. One exception is the atmosphere opacity, which exerts first-order controls on the surface pressure and temperature (Ikoma & Genda, 2006) and therefore affects the amount of ingassing. In our

OLSON AND SHARP 9 of 18

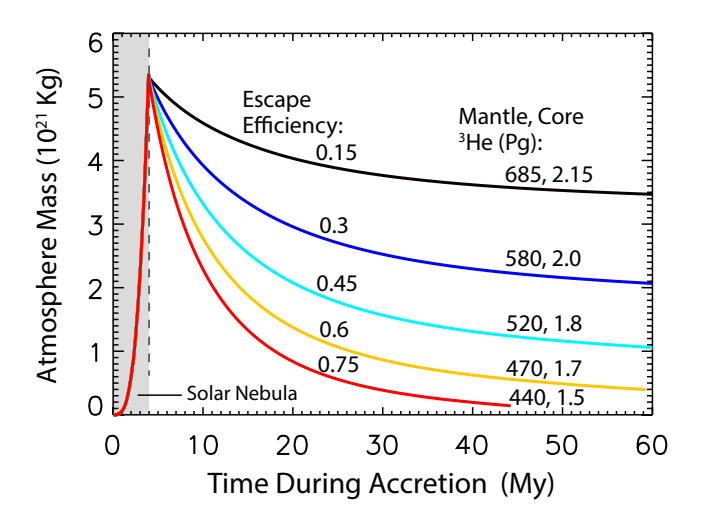


Figure 6. Atmosphere mass (below the photosphere) during accretion for various hydrodynamic escape efficiency factors β . Other energy inputs and parameters are the same as in Figures 2–4. Ingassed ³He abundances in the proto-mantle and proto-core are shown for each case.

model, ingassing varies inversely as the square root of opacity. In addition to opacity, other studies have demonstrated that the primordial atmosphere history is strongly dependent on the hydrodynamic escape efficiency parameter β (Genda & Ikoma, 2008; Erkaev et al., 2016). In Figure 5 we have used $\beta = 0.15$, which is nominal value for energy-limited escape (Hunten et al., 1987). In reality this parameter may be substantially larger (Kuramoto et al., 2013), particularly because large impacts can boost the effective rate of hydrodynamic escape (Ginsburg et al., 2016).

As a test of our model sensitivity to atmosphere escape efficiency, we show in Figure 6 the growth and erosion history of the atmosphere mass for various values of β , with all other parameters the same as in Figures 2–4. We also list in Figure 6 the amounts of ${}^{3}\text{He}$ dissolved in the mantle and core for each choice of β . Although the erosion history of the atmosphere depends strongly on the hydrodynamic escape efficiency, Figure 6 indicates that helium acquisition is not so sensitive to this parameter, decreasing by less than a factor of two between $\beta = 0.15$ and 0.75 in both the proto-mantle and proto-core. This reduced sensitivity is due to the fact that much of the ${}^{3}\text{He}$ acquisition in our model occurs in the first few million years of accretion, before the full effects of atmosphere erosion are felt.

5. Degassing Model

For ³He abundances in the post-accretion Earth, we use a degassing model that tracks the ³He content of the mantle and core with time reversed, starting from present-day conditions and continuing backward to the end

Core 3He

Core Temperature

Core Temperature

Core Temperature

Core Temperature

Figure 7. ³He degassing model. Layers include core, mantle and ocean crust denoted by subscripts c, m, and MORB, respectively, with subscripts s and cmb denoting Earth surface and core-mantle boundary, respectively. ³He concentrations and fluxes denoted by C and F, respectively, with P0 and P1 denoting heat fluxes and boundary layer temperature changes, respectively. P1 denotes the liquid metal-solid silicate partition coefficient for ³He at the CMB. Mantle and core temperature profiles are shown with adiabats removed.

of accretion. Degassing of helium in the post-accretion Earth is controlled by subsolidus mantle convection (Van Keken & Ballentine, 1998). Here we exploit the similarity between heat and helium transport by mantle convection, deriving expressions for the ³He flux at the surface and at the CMB in terms of the heat fluxes at each boundary. This allows us to link the post-accretion history of ³He exchanges between the core and mantle to their coupled thermal evolution.

Figure 7 illustrates the main elements of our degassing model. Evolution equations for the average 3 He concentrations in the core and mantle, C_c and C_m , can be written using the same notation and sign conventions for the boundary fluxes F_s and F_{cmb} that we used for ingassing:

$$M_c \frac{dC_c}{dt} = -F_{cmb} \tag{17}$$

and

$$M_m \frac{dC_m}{dt} = F_{cmb} - F_s \tag{18}$$

where M_c and M_m are the post-accretion masses of the core and mantle, both constant. In the same way, let C_c' denote the mantle concentration of 3 He that was originally deposited in the core by ingassing, and let C_m' denote the mantle concentration of 3 He that was originally deposited in the mantle by ingassing. These concentrations evolve with time according to

$$M_m \frac{dC_c'}{dt} = F_{cmb} - \frac{C_c'}{C_m' + C_c'} F_s \tag{19}$$

and

OLSON AND SHARP 10 of 18

$$M_m \frac{dC_m'}{dt} = -\frac{C_m'}{C_m' + C_c'} F_s. \tag{20}$$

The quantity C'_c/C'_m , which we refer to as the C/M ratio, represents the portion of 3 He in the mantle at any time that originated in the core relative to the portion that originated in the mantle, and is a measure of how much of the mantle 3 He content came from the core.

In order to solve Equations 17–20 backward in time (that is, forward in age τ) we need starting conditions, in this case the present-day ($\tau=0$) mantle and core ³He concentrations C_m (0) and C_c (0). We also need values for the present-day surface and CMB ³He fluxes F_s (0) and F_{cmb} (0), along with expressions for how these fluxes varied in the past.

Among these quantities, the present-day surface flux $F_s(0)$ is the best constrained. The present-day ³He flux from the mantle includes the 527 mol/y MORB flux (Bianchi et al., 2010) plus contributions from other magmatic systems, including OIB, back arc basins, and extensional zones on continents. Although these additional ³He sources are poorly constrained in comparison with MORB, estimates indicate their contributions are relatively minor. For example, Porcelli and Halliday (2001) estimate 13 mol/y from OIB and Van Keken et al. (2001) estimate 47 mol/y from continental extension zones based on ⁴He fluxes there. Including an additional 13 mol/y from back arcs and subduction zones implies $F_s(0) \simeq 600 \text{ mol/y} = 1.8 \text{ kg/y}$, with an uncertainty of at least 25%.

There are also some observational constraints on the present-day mantle ${}^3\text{He}$ concentration, but unfortunately these are weaker. Using the method of Porcelli and Elliott (2008) for example, a mantle abundance can be estimated from MORB production and ${}^3\text{He}$ flux statistics. The ratio of the MORB ${}^3\text{He}$ flux to MORB mass flux $(6 \times 10^{12} \text{ kg/y})$ yields an ${}^3\text{He}$ concentration in newly formed MORB of 2.6×10^{-14} kg/kg. Assuming a helium enrichment factor of $e_{\text{He}} = 10$ between new MORB and its mantle source implies C_m (0) = 2.6×10^{-15} kg/kg, equivalent to 10 Tg of mantle ${}^3\text{He}$. This probably represents a lower bound estimate, because it assumes the MORB source is representative of the whole mantle, the enrichment factor is large, and that helium recycling is negligible. Nevertheless, it highlights the need for a deep source region. If limited to the upper mantle, this concentration would supply the present-day surface ${}^3\text{He}$ flux for less than 1.5 Gy. As for an upper bound, Halliday (2013) uses isotope systematics to obtain far higher estimates for the present-day mantle ${}^3\text{He}$ abundance, ranging from 30 to 300 Tg, equivalent to C_m (0) = 7.8– 78×10^{-15} kg/kg. Taken together, these diverse estimates indicate that the true uncertainty in the present-day mantle ${}^3\text{He}$ concentration is at least $10 \times$, and possibly more. Accordingly, we treat the present-day mantle ${}^3\text{He}$ concentration as a modeling parameter, varying C_m (0) over this range.

The present-day 3 He concentration in the core and the present-day 3 He flux at the CMB are the starting conditions for which the observational constraints are lacking. However, they can be linked to the heat flux at the CMB using boundary layer concepts, as follows. The fluxes of heat Q_{cmb} and 3 He across boundary layers on the mantle side of the CMB can be written as

$$Q_{cmb} = \rho_m c_m \Delta T_{cmb} A_{cmb} v_Q \tag{21}$$

and

$$F_{cmb} = \rho_m \Delta C_{cmb} A_{cmb} v_{He}. \tag{22}$$

Here $A_{\rm cmb}$ is the CMB surface area, $\Delta T_{\rm cmb}$ and $\Delta C_{\rm cmb}$ are the temperature and $^3{\rm He}$ variations across the mantleside boundary layers, ρ_m and c_m are density and specific heat in the solid mantle, and v_Q and $v_{\rm He}$ are the transfer velocities for each species. Diffusion is likely the dominant exchange mechanism at the CMB because the vast differences in density and viscosity between the solid lower mantle and fluid outer core tend to inhibit advective exchange. The transfer velocities for diffusion can be written in terms of the average CMB age $\bar{\tau}_{cmb}$, defined as the average length of time a mantle parcel on the CMB has resided there. With this definition

$$v_O = (2\kappa_T / \pi \bar{\tau}_{cmb})^{1/2} \tag{23}$$

and

OLSON AND SHARP 11 of 18

$$v_{He} = (2\kappa_{He}/\pi\bar{\tau}_{cmb})^{1/2},\tag{24}$$

where κ_T is thermal diffusivity and κ_{He} is helium diffusivity, both in the mantle. Combining Equations 21–24 yields the following relationship between CMB ³He and heat fluxes:

$$F_{cmb} = \left(\frac{\kappa_{He}}{\kappa_T}\right)^{1/2} \frac{\Delta C_{cmb}}{\Delta T_{cmb}} \left(\frac{Q_{cmb}}{c_m}\right). \tag{25}$$

Chemical equilibrium at the CMB implies

$$\Delta C_{cmb} = \frac{C_c}{D_{ls}} - C_m,\tag{26}$$

where D_{ls} is the liquid metal-solid silicate partition coefficient for helium. Substituting Equation 26 into Equation 25 yields a relationship between the ³He concentration in the core and ³He flux at the CMB and in terms of the mantle ³He concentration, the flux heat at the CMB, and the basal mantle thermal boundary layer temperature increase. For present-day conditions, this is just

$$C_c(0) = D_{ls} \left(C_m(0) + \left(\frac{\kappa_T}{\kappa_{He}} \right)^{1/2} \frac{c_m \Delta T_{cmb}(0)}{Q_{cmb}(0)} F_{cmb}(0) \right). \tag{27}$$

In addition, the variation of Equation 25 with age can be written in terms of present-day quantities as

$$\frac{F_{cmb}(\tau)}{F_{cmb}(0)} = \frac{\Delta C_{cmb}(\tau)}{\Delta C_{cmb}(0)} \frac{\Delta T_{cmb}(0)}{\Delta T_{cmb}(\tau)} \frac{Q_{cmb}(\tau)}{Q_{cmb}(0)},\tag{28}$$

where we have assumed the mantle material properties do not change with time.

A different parameterization is required at the top of the mantle, where subsolidus convection, melting, and hydrothermal transport combine to produce the surface 3 He flux. Data from several oceanic spreading centers yield an average value for the proportionality between 3 He flux and hydrothermal heat flux of about 180 mol/y of 3 He flux per hydrothermal TW (Torgersen, 1993). Hydrothermal heat flux at spreading centers contributes about 11% to the total oceanic heat flux (Stein & Stein, 1994), which implies approximately 20 mol/y of 3 He flux per oceanic TW of heat. Using 30 TW for the present-day oceanic part of the global heat flux, this corresponds to $F_s(0) \simeq 600$ mol/y, equal to our estimate of the present-day global 3 He flux and within the error bars of the Bianchi et al. (2010) determination of the present-day MORB flux.

However, this simple proportionality between heat and helium flux is not adequate for extrapolation in time, because it omits the dependence on mantle helium concentration and other time variable factors. If instead we assume that the advective transport of mantle helium is similar to the advective transport of mantle heat, then the surface 3 He flux also depends on the mantle potential temperature T_{mp} and heat capacity c_{m} , in addition to mantle 3 He concentration and heat flux. Dimensional analysis applied to this larger set of parameters implies

$$F_s \sim \frac{C_m Q_m}{c_m T_{mn}},\tag{29}$$

which can be converted into a proportionality like (28) for the age dependence of the surface ³He flux:

$$\frac{F_s(\tau)}{F_s(0)} = \frac{C_m(\tau)}{C_m(0)} \frac{T_{mp}(0)}{T_{mp}(\tau)} \frac{Q_m(\tau)}{Q_m(0)}.$$
(30)

Our degassing calculations proceed as follows. We fix the present-day surface 3 He flux at $F_{s}(0) = 600$ mol/y (1.8 kg/y) in all cases and choose either 10, 30, and 100 Tg for the present-day mantle 3 He abundance, which specifies $C_{m}(0)$. We then select an arbitrary present-day CMB 3 He flux $F_{cmb}(0)$ and evaluate Equation 27 for the corresponding present-day core 3 He concentration $C_{c}(0)$, using the properties in Table 2. For the liquid metal-solid silicate partition coefficient we use $D_{ls} = 10$ and 1, the larger value from experiments by (Roth et al., 2019) on 3 He partitioning between liquid FeS and olivine at upper mantle conditions, the smaller value an extrapolation

OLSON AND SHARP 12 of 18

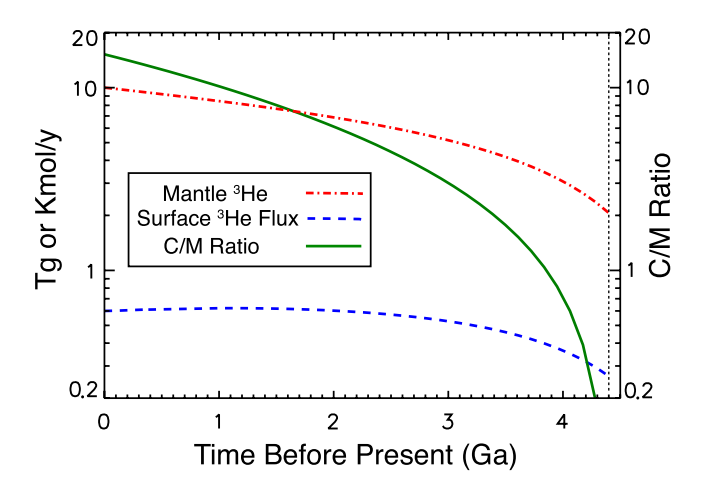


Figure 8. Degassing history, showing reversed time evolution of mantle ³He abundance, surface ³He flux, and the C/M ratio for present-day mantle and core abundances of 10 Tg and 2.3 Pg, respectively, partition coefficient $D_{\rm ls} = 1$, and 1,130 mol/y flux at the core-mantle boundary. Dashed line at 4.4 Ga denotes the nominal onset of degassing by mantle convection.

to the higher temperatures of the lower mantle in the deep past. With the above starting conditions we integrate Equations 17 and 18 backward in time from $\tau=0$ to 4.4 Ga, which we take as the nominal age for the end of accretion and onset of mantle convective degassing. In all of these calculations we adopt an idealized thermal history, in which the mantle surface heat flux increases linearly with age by a factor of two at 4.4 Ga, starting at a present-day value of Q_m (0) = 32 TW (Jaupart et al., 2015). For the heat flux at the CMB, we use a constant value $Q_{\rm cmb}=13$ TW (Nimmo, 2015), plus constant values $T_{\rm mp}=1600$ K and $\Delta T_{\rm cmb}=1200$ K, along with a very conservative value for helium diffusivity in the lower mantle, $\kappa_{\rm He}=1\times 10^{-10}$ m²/s. We then integrate Equations 19 and 20 forward in time starting from 4.4 Ga to the present-day, using $C_c'=0$ and $C_m'=C_m(4.4$ Ga) as the starting conditions. This second integration tracks the amounts of mantle ³He that originated in the core and mantle and allows us to construct the C/M ratio.

As a test of the reliability of this degassing model, we performed a separate set of calculations with the core ³He flux set to zero and the mantle thermal history and initial mantle ³He concentrations adjusted to match those used by Van Keken and Ballentine (1998) and Van Keken et al. (2001). We find that our degassing model results agree with theirs to within 15% for degassing by whole mantle convection with uniform viscosity and to within 20% for layered viscosity. This agreement, in spite of the vast differences in mode-

ling approaches—boundary layer flux parameterizations in our case versus high-resolution 2D thermo-chemical convection with particle tracking in theirs—provides evidence that our approach captures the overall rate of ³He degassing expected for mantle convection.

6. Degassing Results

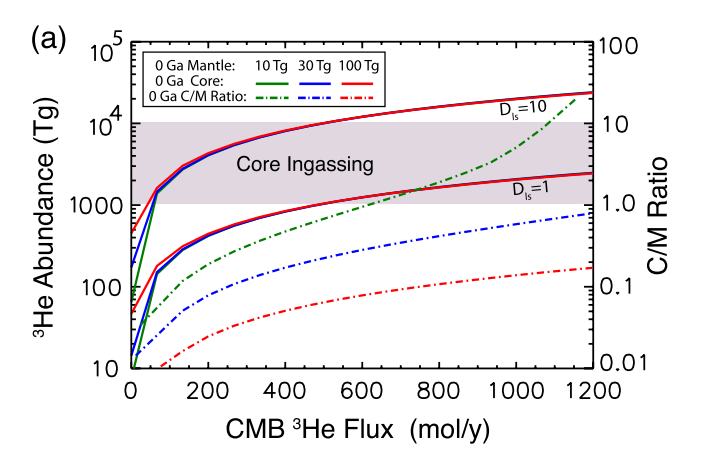
Figure 8 shows results from a degassing calculation that starts with a 10 Tg present-day mantle 3 He abundance, 600 mol/y for the present-day surface 3 He flux, a present-day 3 He flux of 1,130 mol/y applied at the CMB, and $D_{ls} = 1$. This combination of properties and starting conditions yields a present-day core 3 He abundance of 2.3 Pg, consistent with Figure 5 abundances delivered to the core by nebular ingassing. As shown in Figure 8, the mantle abundance and flux both decrease gradually with age, before decreasing more sharply around 4 Ga. At 4.4 Ga, the nominal end of accretion and onset of mantle convection in this calculation, the 3 He abundance in the mantle is just 2 Tg. Comparing this to the abundances in Figure 5 implies a very efficient (>99%) 3 He loss from the early mantle, prior to convective degassing. In contrast, the 3 He abundance in the core and the 3 He flux across the CMB change by only a few percent between 0 and 4.4 Ga, consistent with the core being the reservoir that has replenished the mantle with 3 He, possibly increasing the mantle abundance over time.

The C/M ratio in Figure 8 grows with time (decreases with age), exceeding 10 at 1 Ga and 12 at 0 Ga, implying that, for this particular set of conditions, more than 90% of the ³He in the present-day mantle was originally deposited in the core and later leaked across the CMB. Furthermore, much of this leakage would have occurred in the deep past. According to Figure 8, the C/M ratio exceeds 1 before 3.8 Ga, implying that more than one half of the ³He in the mantle at that time came from the core.

Figure 9 summarizes the broader systematics of our degassing model for two choices of the metal-silicate partition coefficient at the CMB. In these calculations the present-day (0 Ga) surface ³He flux is again fixed at 600 mol/y, while the present-day flux across the CMB is varied from zero to a maximum of 1,200 mol/y. Figure 9a shows the present-day core abundance and the present-day C/M ratio for three choices of the present-day mantle abundance: 10, 30, and 100 Tg, respectively. Figure 9b shows the core and mantle abundances at 4.4 Ga for these same present-day choices. Shading in both panels indicates the range of core ³He abundance from nebular ingassing according to Figure 5.

OLSON AND SHARP 13 of 18





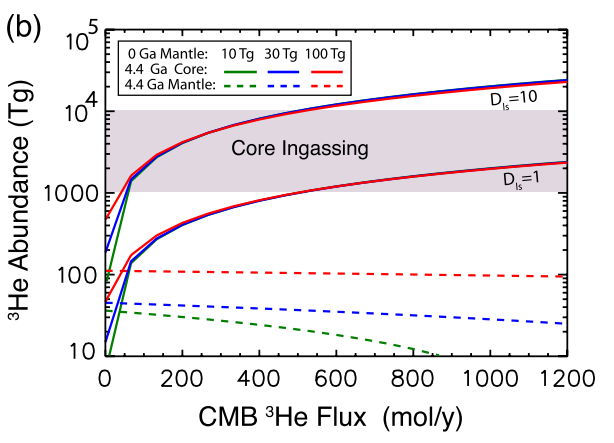


Figure 9. Degassing systematics. 3 He abundances in the mantle and core versus present-day 3 He flux at the CMB. Colors denote representative 0 Ga (present-day) mantle 3 He abundances. Solid curves in (a) and (b) denote 0 Ga (present-day) and 4.4 Ga core 3 He abundances, respectively, for different values of the core-mantle partition coefficient D_{ls} . Dash-dot curves in (a) denote present-day C/M ratios. Dashed curves in (b) denote 4.4 Ga mantle abundances, the nominal onset of degassing by subsolidus mantle convection in our model. Shadings indicate the range of 3 He acquired by the core from nebular ingassing, according to Figure 5.

All of the cases on the right-hand side of Figures 9a and 9b yield core 3 He abundances of one or more petagrams at 0 Ga and also at 4.4 Ga, consistent with our ingassing results. This regime is characterized by severe 3 He depletion of the early mantle, as indicated by the dashed curves in Figure 9b. In this regime the C/M ratio is larger than one if the present-day mantle abundance is 10 Tg or less, and for these cases most of the 3 He now in the mantle came from the core. The $D_{ls}=1$ cases on the left-hand side of Figures 9a and 9b are acceptable solutions, but these entail far less core 3 He and are therefore inconsistent with our ingassing model predictions. Many of these cases also have small C/M ratios, implying only minor contamination of mantle 3 He from the core.

The dividing line between the two regimes approximately corresponds to a CMB ³He flux equal to or slightly greater than the present-day surface ³He flux, that is, 600–800 mol/y in Figure 9. If the CMB flux is near this dividing line, then surface losses are more-or-less compensated by ³He diffusing from the core, and the present-day mantle is in an approximate statistical steady state with respect to ³He content. If the present-day mantle contains 30 Tg ³He, this statistical steady state implies that about one quarter of what is now in the mantle came from the core, whereas if the present-day mantle contains 10 Tg, about one half of that came from the core. In contrast, with 100 Tg ³He in the present-day mantle, Figure 9a indicates that only about a tenth came from the core.

Figure 10 shows the total (cumulative) ³He lost from the mantle and core input into the mantle since 4.4 Ga, the nominal onset of mantle convection in our degassing model, as functions of the present-day CMB ³He flux, for the same three present-day mantle ³He abundance choices in Figure 9. The values and trends in Figure 10 are consistent with the results of previous mantle degassing studies (Gonnermann & Mukhopadhyay, 2009; Van Keken & Ballentine, 1998; Van Keken et al., 2001) in finding that subsolidus convection removes at most a few tens of teragrams of ³He from the mantle, even allowing for higher rates of MORB production in the deep past. Similarly, ³He input to the mantle from the core over the same time period is a few tens of teragrams at most. Nevertheless, Figure 10 indicates that if the present-day CMB ³He flux is above 800 mol/y, replenishment from the core exceeds what the mantle has lost since 4.4 Ga.

7. Discussion

Our ingassing and degassing calculations identify conditions under which the core could have acquired of order 1 Pg of ³He during accretion, and then leak a portion of that back into the mantle. If the early mantle was helium depleted, our results indicate that much of the ³He now in the mantle once resided in the core. This differs from most interpretations of the high ³He/⁴He-ratios found in some mantle plume-derived OIB (Mukhopadhyay & Pari, 2019) and in some transition zone diamonds (Timmerman et al., 2019), in which the ³He is inferred to have come from deep mantle reservoirs (Gonnermann & Mukhopadhyay, 2009), with the seismically detected Large Low Shear Velocity Provinces in the lowermost mantle (LLSVPs; Garnero et al. (2016) being favored candidates (M. Jackson et al., 2017; Williams et al., 2019). LLSVPs are plausible source regions for ³He because these structures appear to have retained their identity in the mantle for hundreds of millions of years or more (Torsvik et al., 2012), and in addition, mantle plume trajectories calculated from the locations of high ³He/⁴He hotspot OIB tend to converge around the LLSVPs (Williams et al., 2019).

There are, however, subtle complications with the LLSVPs being the only reservoirs enriched in ³He in the deep Earth. For one, high-resolution numerical simulations (M. Li et al., 2018; Heyn et al., 2020) reveal that mantle plumes forming around dense LLSVP-type structures entrain relatively little material from those structures.

OLSON AND SHARP 14 of 18

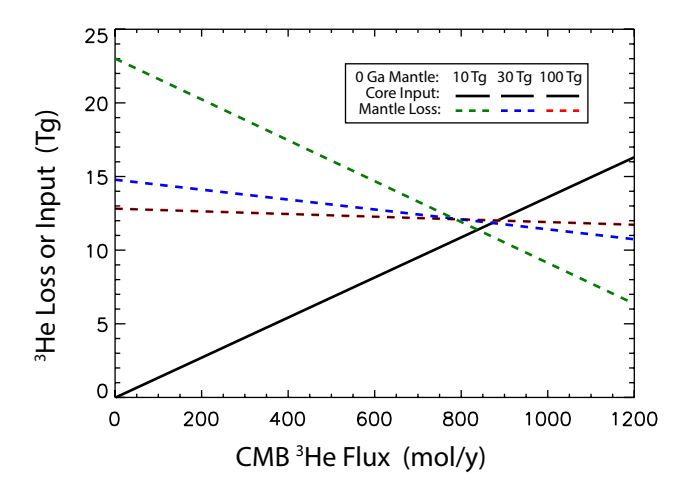


Figure 10. Cumulative (4.4–0 Ga) ³He loss from the mantle and input to the mantle from the core versus present-day ³He flux at the CMB. Colors denote representative 0 Ga (present-day) mantle ³He abundances.

Instead, the plumes in these simulations consist mostly of mantle material drawn from the highest temperature part of the basal thermal boundary layer, that is, regions located directly above the CMB and away from LLSVP structures. These are precisely the locations where helium is expected to leak most vigorously from the core. A related complication is the observed correlation between high ³He/⁴He and high potential temperatures in mantle plumes (M. Jackson et al., 2017; Willhite et al., 2019), which suggests that the closer plumes form to the core, the more likely they are to be enriched in ³He.

Putting it another way, long-lived volatile reservoirs in the deep mantle do not preclude the core as a source of primordial ³He, nor vice-versa. Instead, the main requirements for the core to be a major source of ³He are (a) abundant dissolution into a magma ocean with helium partitioning between the magma and core-forming metals, (b) early and efficient helium depletion from the mantle interior, and (c) ³He flux across the CMB. The sequence of events consisting of nebular ingassing followed by catastrophic Moon-formation followed by degassing by deep mantle convection provides for all three requirements, and is broadly consistent with current interpretations of Earth history. Accordingly, helium may not be the only light volatile leaking from the core. Although recent experiments are somewhat equivocal on hydrogen

partitioning (Clesi et al., 2018; Malavergne et al., 2019; Tagawa et al., 2021), molecular dynamics calculations (Y. Li et al., 2020) indicate that hydrogen dissolved in silicate melt partitions strongly into iron liquid, suggesting that the core may contain abundant hydrogen. If so, hydrogen transfer from core to mantle will have the effect of reducing FeO to Fe metal, which could then be added to the core.

The processes by which volatiles and other lighter constituents are added to and then leak from the core have ramifications that go far beyond Earth's volatile budget. Elements such as magnesium and silicon that are weakly soluble in iron near its melting point tend to become more soluble at higher temperatures, allowing them to dissolve into the high temperature proto-core (Badro et al., 2018). After accretion, as mantle convection cools the core, these lighter elements are expected to exsolve at the top of the core, creating negative buoyancy in the residual core liquid and providing a source of energy to drive the early geodynamo. In order for this mechanism to operate efficiently, the lighter elements must exit the core and become incorporated into the overlying mantle (Mittal et al., 2020), which implies exchange mechanisms across the CMB similar to those described here for helium. In addition to a loss of lighter elements from the core, it has been proposed that variability of tungsten isotopic ratios in OIB reflects their long-term sequestration in the core and slow release into the mantle (Rizo et al., 2019) or alternatively, localized core-mantle equilibration (Mundl-Petermeier et al., 2020).

Heavier noble gases may also have been deposited in the core along with helium, and offer independent ways to test for core sequestration and core leaking. For example, ¹²⁹Xe may have been produced in the core after accretion by decay of its parent isotope ¹²⁹I, since iodine tends toward siderophile behavior at high pressures (C. Jackson et al., 2018) and may have been deposited in the core during accretion. However, magma ocean mixing of stable and unstable isotopes with diverse metal/silicate affinities is a complex dynamical phenomenon (Deguen et al., 2014; Landeau et al., 2021) and requires additional constraints and assumptions beyond those used here for primordial helium.

Lastly, it is important to highlight the large number of caveats that apply to this model. To begin with, three particulars of Earth formation are necessary: protoplanet growth in the presence of nebular gas, helium partitioning into core-forming metals, and efficient degassing of the early mantle. Individually, each of these particulars is reasonably probable, but the combination of all three is less so. Furthermore, major uncertainties abound, including the lifetime of the solar nebula relative to the accretion rate, the role of pebbles versus planetesimals, nebular atmosphere opacity, the erosion rate of the atmosphere, helium partition coefficients and diffusivities at high pressure and temperature, and the effects of giant impacts, just to name a few. Taken jointly, the net effect of these uncertainties is probably in the direction of reducing the absolute amounts of sequestered helium, compared to what our model predicts. However, provided the sum of these uncertainties does not fundamentally alter the relative amounts of helium retained by the mantle and core, then our primary result—that the core is a major source of primordial helium—will still hold.

OLSON AND SHARP 15 of 18



Data Availability Statement

Primary data were not used, nor created for this research.

Acknowledgments

This work was partially supported by grants EAR1135382 and EAR1953992 from the National Science Foundation. We thank John Hernlund and Marc Hirschmann for their constructive reviews.

References

- Anzellini, S., Dewaele, A., Mezouar, M., Loubeyre, P., & Morard, G. (2013). Melting of iron at Earth's inner core boundary based on fast X-ray diffraction. Science, 340, 464–466. https://doi.org/10.1126/science.1233514
- Badro, J., Aubert, J., Hirose, K., Nomura, R., Blanchard, I., Borensztajn, S., & Siebert, J. (2018). Magnesium partitioning between Earth's mantle and core and its potential to drive an early exsolution geodynamo. *Geophysical Research Letters*, 45, 13240–13248. https://doi. org/10.1029/2018GL080405
- Bania, T., Rood, R., & Baiser, D. (2002). The cosmological density of baryons from observations of ³He+ in the Milky Way. *Nature*, 415, 54–57. https://doi.org/10.1038/415054a
- Bianchi, D., Sarmiento, J., Gnanadesikan, A., Key, R. M., Schlosser, P., & Newton, R. (2010). Low helium flux from the mantle inferred from simulations of oceanic helium isotope data. Earth and Planetary Science Letters, 297, 379–386. https://doi.org/10.1016/j.epsl.2010.06.037
- Biersteker, J., & Schlichting, H. (2021). Losing oceans: The effects of composition on the thermal component of impact-driven atmospheric loss. Monthly Notices of the Royal Astronomical Society, 501, 587–595.
- Bouhifd, M., Jephcoat, A., Heber, V., & Kelley, S. (2013). Helium in Earth's early core. *Nature Geoscience*, 6, 982–986. https://doi.org/10.1038/ngeo1959
- Canup, R. (2012). Forming a moon with an Earth-like composition via a giant impact. Science, 227, 1052–1055. https://doi.org/10.1126/science.1226073
- Carter, P., Lock, S., & Stewart, S. (2020). The energy budgets of giant impacts. Journal of Geophysical Research: Planets, 125, 006042. https://doi.org/10.1029/2019je006042
- Clesi, V., Bouhifd, M. A., Bolfan-Casanova, N., Manthilake, G., Schiavi, F., Raepsaet, C., & Andrault, D. (2018). Low hydrogen contents in the cores of terrestrial planets. *Science Advances*, 4(3), e1701876. https://doi.org/10.1126/sciadv.1701876
- Cuk, M., & Stewart, S. (2012). Making the moon from a fast-spinning Earth: A giant impact followed by resonant despinning. Science, 338, 1047–1052. https://doi.org/10.1126/science.1225542
- 1047–1052. https://doi.org/10.1126/science.1225542

 Deguen, R., Landeau, M., & Olson, P. (2014). Turbulent metal-silicate mixing, fragmentation, and equilibration in magma oceans. *Earth and*
- Planetary Science Letters, 391, 274–287. https://doi.org/10.1016/j.epsl.2014.02.007 deKoker, N., & Stixrude, L. (2009). Self-consistent thermodynamic description of silicate liquids, with application to shock melting of MgO
- periclase and $MgSiO_3$ perovskite. Geophysical Journal International, 178, 162–179. https://doi.org/10.1111/j.1365-246x.2009.04142.x Dygert, N., Jackson, C., Hesse, M., Tremblay, M. M., Shuster, D. L., & Gu, J. T. (2018). Plate tectonic cycling modulates Earth's ${}^{3}He/{}^{2}Ne$ ratio.
- Earth and Planetary Science Letters, 498, 309–321. https://doi.org/10.1016/j.epsl.2018.06.044

 Elkins-Tanton, L. (2011). Formation of early water oceans on rocky planets. Astrophysics and Space Science, 332, 359–364. https://doi.org/10.1007/s10509-010-0535-3
- Elkins-Tanton, L. (2012). Magma oceans in the inner solar system. Annual Review of Earth and Planetary Sciences, 40, 113–139. https://doi.org/10.1146/annurev-earth-042711-105503
- Erkaev, N., Lammer, H., Odert, P., Kislyakova, K. G., Johnstone, C. P., Güdel, M., & Khodachenko, M. L. (2016). EUV-driven mass-loss of protoplanetary cores with hydrogen-dominated atmospheres: The influences of ionization and orbital distance. *Monthly Notices of the Royal Astronomical Society*, 460, 1300–1309. https://doi.org/10.1093/mnras/stw935
- Erkaev, N., Lammer, H., Odert, P., Kulikov, Y. N., Kislyakova, K. G., Khodachenko, M. L., et al. (2013). XUV-exposed, non-hydrostatic hydrogen-rich upper atmospheres of terrestrial planets. Part I: Atmospheric expansion and thermal escape. *Astrobiology*, 13, 1011–1029. https://doi.org/10.1089/ast.2012.0957
- Garnero, E., McNamara, A., & Shim, S.-H. (2016). Continent-sized anomalous zones with low seismic velocity at the base of Earth's mantle. Nature Geoscience, 9, 481–489. https://doi.org/10.1038/ngeo2733
- Genda, H., & Ikoma, M. (2008). Origin of the ocean on the Earth: Early evolution of water D/H in a hydrogen-rich atmosphere. *Icarus*, 194, 42–52. https://doi.org/10.1016/j.icarus.2007.09.007
- Ginsburg, S., Schlichting, H., & Sari, R. (2016). Super-Earth atmospheres: Self-consistent gas accretion and retention. *Journal of Astrophysics*, 825, 29. https://doi.org/10.3847/0004-637X/825/1/29
- Gonnermann, H., & Mukhopadhyay, S. (2009). Preserving noble gases in a convecting mantle. Nature, 459, 560–563. https://doi.org/10.1038/nature08018
- Halliday, A. (2013). The origins of volatiles in the terrestrial planets. Geochem. Cosmochem. Acta, 105, 146–171. https://doi.org/10.1016/j.gca.2012.11.015
- Hansen, B. (2009). Formation of the terrestrial planets from a narrow annulus. *The Astrophysical Journal*, 703, 1131–1140. https://doi.org/10.1088/0004-637x/703/1/1131
- Heyn, B., Conrad, C., & Tronnes, R. (2020). Core-mantle boundary topography and its relation to the viscosity structure of the lowermost mantle. Earth and Planetary Science Letters, 543, 116358. https://doi.org/10.1016/j.epsl.2020.116358
- Hunten, D., Pepin, R., & Walker, J. (1987). Mass fractionation in hydrodynamic escape. Icarus, 69, 532–549. https://doi.org/10.1016/0019-1035(87)90022-4
- Ikoma, M., & Genda, H. (2006). Constraints on the mass of a habitable planet with water of nebular origin. *The Astrophysical Journal*, 648, 696–706. https://doi.org/10.1086/505780
- Jackson, C., Bennett, N., Du, Z., Cottrell, E., & Fei, Y. (2018). Early episodes of high-pressure core formation preserved in plume mantle. *Nature*, 553, 491–495. https://doi.org/10.1038/nature25446
- Jackson, M., Konter, J., & Becker, T. (2017). Primordial helium entrained by the hottest mantle plumes. *Nature*, 542, 340–343. https://doi.org/10.1038/nature21023
- Jaupart, C., Labrosse, S., & Mareschal, J. (2015). Temperatures, heat and energy in the mantle of the Earth. In G. Schubert (Ed.), Treatise on geophysics (2nd ed., Vol. 6). Elsevier. https://doi.org/10.1016/b978-0-444-53802-4.00126-3
- Jephcoat, A. (1998). Rare-gas solids in the Earth's deep interior. Nature, 393, 355–358. https://doi.org/10.1038/30712
- Johansen, A., Ronnet, T., Bizzarro, M., & Schiller, M. (2021). Pebble accretion model for the formation of the terrestrial planets in the solar system. Science Advances, 7, 0444. https://doi.org/10.1126/sciadv.abc0444

OLSON AND SHARP 16 of 18



- Kleine, T., & Rudge, J. (2011). Chronometry of meteorites and the formation of the Earth and moon. *Elements*, 7, 41–46. https://doi.org/10.2113/gselements.7.1.41
- Kleine, T., & Walker, R. (2017). Tungsten isotopes in planets. Annual Review of Earth and Planetary Sciences, 45, 389–417. https://doi.org/10.1146/annurev-earth-063016-020037
- Kuramoto, K., Umemoto, T., & Ishiwatari, M. (2013). Effective hydrodynamic escape from an early Earth atmosphere inferred from high-accuracy numerical simulation. Earth and Planetary Science Letters, 375, 312–318. https://doi.org/10.1016/j.epsl.2013.05.050
- Kurz, M., Jenkins, W., & Hart, S. (1982). Helium isotope systematics of oceanic islands and mantle heterogeneity. Nature, 297, 42–46. https://doi.org/10.1038/297043a0
- Lambrechts, M., & Johansen, A. (2012). Rapid growth of gas-giant cores by pebble accretion. Astronomy and Astrophysics, 544, 13. https://doi.org/10.1051/0004-6361/201219127
- Lammer, H., Kasting, J., Chassefière, E., Johnson, R. E., Kulikov, Y. N., & Tian, F. (2008). Atmospheric escape and evolution of terrestrial planets and satellites. Space Science Reviews, 139, 399–436. https://doi.org/10.1007/s11214-008-9413-5
- Lammer, H. A., Stökl, N., Dorfi, E., Odert, P., Güdel, M., Kulikov, Y. N., et al. (2014). Origin and loss of nebula-captured hydrogen envelopes from sub- to super-Earths in the habitable zone of sun-like stars. *Monthly Notices of the Royal Astronomical Society*, 439, 3225–3238. https://doi.org/10.1093/mnras/stu085
- Landeau, M., Deguen, R., Phillips, D., Neufeld, J., Lherm, V., & Dalziel, S. (2021). Metal-silicate mixing by large Earth-forming impacts. Earth and Planetary Science Letters, 564, 116888. https://doi.org/10.1016/j.epsl.2021.116888
- Levison, H., Kretke, K., Walsh, K., & Bottke, W. F. (2015). Growing the terrestrial planets from the gradual accumulation of sub-meter-sized objects. *Proceedings of the National Academy of Sciences of the United States of America*, 112, 14180–14185. https://doi.org/10.1073/pnas.1513364112
- Li, M., Zhong, S., & Olson, P. (2018). Linking lowermost mantle structure, core-mantle boundary heat flux and mantle plume formation. *Physics of the Earth and Planetary Interiors*, 277, 10–29. https://doi.org/10.1016/j.pepi.2018.01.010
- Li, Y., Vocadlo, L., Sun, T., & Brodholt, J. (2020). The Earth's core as a reservoir of water. Nature Geoscience, 13, 453–458. https://doi.org/10.1038/s41561-020-0578-1
- Lupton, J., & Craig, H. (1975). Excess ³He in oceanic basalts: Evidence for terrestrial primordial helium. Earth and Planetary Science Letters, 26, 133–139. https://doi.org/10.1016/0012-821x(75)90080-1
- Lupton, J., Weiss, R., & Craig, H. (1977). Mantle helium in hydrothermal plumes in the Galapagos Rift. *Nature*, 267, 603–604. https://doi.org/10.1038/267603a0
- Malavergne, V., Bureau, H., Raepsaet, C., Gaillard, F., Poncet, M., Surble, S., et al. (2019). Experimental constraints on the fate of H and C during planetary core-mantle differentiation. Implications for the Earth. *Icarus*, 321, 473–485. https://doi.org/10.1016/j.icarus.2018.11.027
- Matsuda, J., Sudo, M., Ozima, M., Ito, K., Ohtaka, O., & Ito, E. (1993). Noble gas partitioning between metal and silicate under high pressures. Science, 259, 788–790. https://doi.org/10.1126/science.259.5096.788
- Melosh, H., & Vickery, A. (1989). Impact erosion of the primordial atmosphere of Mars. Nature, 338(6215), 487–489. https://doi.org/10.1038/338487a0
- Mittal, T., Knezek, N., Arveson, S., McGuire, C. P., Williams, C. D., Jones, T. D., & Li, J. (2020). Precipitation of multiple light elements to power Earth's early dynamo. Earth and Planetary Science Letters, 532, 116030. https://doi.org/10.1016/j.epsl.2019.116030
- Mizuno, H., Nakazawa, K., & Hayashi, C. (1980). Dissolution of the primordial rare gases into the molten Earth's material. Earth and Planetary Science Letters, 50, 202–210. https://doi.org/10.1016/0012-821x(80)90131-4
- Mukhopadhyay, S., & Pari, R. (2019). Noble gases: A record of Earth's evolution and mantle dynamics. *Annual Review of Earth and Planetary Sciences*, 47, 389–419. https://doi.org/10.1146/annurev-earth-053018-060238
- Mundl-Petermeier, A., Walker, R., Fischer, R., Lekic, V., Jackson, M. G., & Kurz, M. D. (2020). Anomalous ¹⁸²W in high ³He/⁴He ocean island basalts: Fingerprints of Earth's core? *Geochimica et Cosmochimica Acta*, 271, 194–211. https://doi.org/10.1016/j.gca.2019.12.020
- Nakajima, M., & Stevenson, D. (2015). Melting and mixing states of the Earth's mantle after the Moon-forming impact. Earth and Planetary Science Letters, 427, 286–295. https://doi.org/10.1016/j.epsl.2015.06.023
- Nimmo, F. (2015). Energetics of the core. In G. Schubert (Ed.), *Treatise on geophysics* (2nd ed., Vol. 8, pp. 27–55). Elsevier. https://doi.org/10.1016/b978-0-444-53802-4.00139-1
- Nimmo, F., Kretke, K., & Ida, S. (2018). Transforming dust to planets. Space Science Reviews, 214. https://doi.org/10.1007/s11214-018-0533-2 Olson, P., & Sharp, Z. (2018). Hydrogen and helium ingassing during terrestrial planet accretion. Earth and Planetary Science Letters, 498, 418–426. https://doi.org/10.1016/j.epsl.2018.07.006
- Olson, P., & Sharp, Z. (2019). Nebular atmosphere to magma ocean: A model for volatile capture during Earth accretion. *Physics of the Earth and Planetary Interiors*, 294, 106294. https://doi.org/10.1016/j.pepi.2019.106294
- Pahlevan, K., & Stevenson, D. (2007). Equilibration in the aftermath of the lunar-forming giant impact. *Earth and Planetary Science Letters*, 262, 438–449. https://doi.org/10.1016/j.epsl.2007.07.055
- Pepin, R., & Porcelli, D. (2006). Xenon isotope systematics, giant impacts, and mantle degassing on the early Earth. Earth and Planetary Science Letters, 250, 470–485. https://doi.org/10.1016/j.epsl.2006.08.014
- Porcelli, D., & Elliott, T. (2008). The evolution of he isotopes in the convecting mantle and the preservation of high ³He/⁴He ratios. *Earth and Planetary Science Letters*, 269, 175–185. https://doi.org/10.1016/j.epsl.2008.02.002
- Porcelli, D., & Halliday, A. (2001). The core as a possible source of mantle helium. Earth and Planetary Science Letters, 192, 45–56. https://doi.org/10.1016/s0012-821x(01)00418-6
- Poreda, R., & Craig, H. (1989). Helium isotope ratios in circum-Pacific volcanic arcs. *Nature*, 338, 473–478. https://doi.org/10.1038/338473a0
 Rizo, H., Andrault, D., Bennett, N., Humayun, M., Brandon, A., Vlastelic, I., et al. (2019). ¹⁸²W evidence for core-mantle interaction in the source of mantle plumes. *Geochemical Perspectives Letters*, 11, 6–11. https://doi.org/10.7185/geochemlet.1917
- Roth, A., Liebske, C., Maden, C., Burton, K., Schönbächler, M., & Busemann, H. (2019). The primordial He budget of the Earth set by percolative core formation in planetesimals. *Geochemical Perspectives Letters*, 9, 26–31. https://doi.org/10.7185/geochemlet.1901
- Sakuraba, H., Kurokawa, H., & Genda, H. (2019). Impact degassing and atmospheric erosion on Venus, Earth, and Mars during the late accretion. *Icarus*, 317, 48–58. https://doi.org/10.1016/j.icarus.2018.05.035
- Sasaki, S. (1999). Presence of a primary solar-type atmosphere around the Earth: Evidence of dissolved noble gas. *Planetary and Space Science*, 47, 1423–1431. https://doi.org/10.1016/s0032-0633(99)00084-7
- Sasaki, S., & Nakazawa, K. (1990). Did a primary solar-type atmosphere exist around the proto-Earth? *Icarus*, 85, 21–42. https://doi.org/10.1016/0019-1035(90)90101-e
- Schiller, M., Bizzarro, M., & Siebert, J. (2020). Iron isotope evidence for rapid accretion and differentiation of the proto-Earth. *Science Advances*, 6, 7604. https://doi.org/10.1126/sciadv.aay7604

OLSON AND SHARP 17 of 18



- Schlichting, H., & Mukhopadhyay, S. (2018). Atmospheric impact losses. Space Science Reviews, 214(34). https://doi.org/10.1007/s11214-018-0471-z
- Sharp, Z. (2017). Nebular ingassing as a source of volatiles to the terrestrial planets. Chemical Geology, 448, 137–150. https://doi.org/10.1016/j.chemgeo.2016.11.018
- Solomatov, V. (2007). Magma oceans and primordial mantle differentiation. In D. Stevenson (Ed.), *Treatise on geophysics* (pp. 91–119). Elsevier. https://doi.org/10.1016/b978-044452748-6.00141-3
- Stein, C., & Stein, S. (1994). Constraints on hydrothermal heat flux through the oceanic lithosphere from global heat flow. *Journal of Geophysical Research*, 99, 3081–3095. https://doi.org/10.1029/93jb02222
- Tagawa, S., Sakamoto, N., Hirose, K., Yokoo, S., Hernlund, J., Ohishi, Y., & Yurimoto, H. (2021). Experimental evidence for hydrogen incorporation into Earth's core. Nature Communications, 12, 1–8. https://doi.org/10.1038/s41467-021-22035-0
- Timmerman, S., Honda, M., Burnham, A., Amelin, Y., Woodland, S., Pearson, D. G., et al. (2019). Primordial and recycled helium isotope signatures in the mantle transition zone. *Science*, 365, 692–694. https://doi.org/10.1126/science.aax5293
- Torgersen, T. (1993). Defining the role of magmatism in extensional tectonics: Helium 3 fluxes in extensional basins. *Journal of Geophysical Research*, 98, 16257–16269. https://doi.org/10.1029/93jb00891
- Torsvik, T., Van Der Voo, R., Preeden, U., Mac Niocaill, C., Steinberger, B., Doubrovine, P. V., et al. (2012). Phanerozoic polar wander, palaeogeography and dynamics. *Earth-Science Reviews*, 114, 325–368. https://doi.org/10.1016/j.earscirev.2012.06.007
- Van Keken, P., & Ballentine, C. (1998). Whole-mantle versus layered mantle convection and the role of a high-viscosity lower mantle in terrestrial volatile evolution. Earth and Planetary Science Letters, 156, 19–32. https://doi.org/10.1016/s0012-821x(98)00023-5
- Van Keken, P., Ballentine, C., & Porcelli, D. (2001). A dynamical investigation of the heat and helium imbalance. Earth and Planetary Science Letters, 188, 421–434. https://doi.org/10.1016/s0012-821x(01)00343-0
- Villeneuve, J., Chaussidon, M., & Libourel, G. (2009). Homogeneous distribution of ²⁶Al in the solar system from the Mg isotopic composition of chondrules. *Science*, 325, 985–988. https://doi.org/10.1126/science.1173907
- Vogt, M., Trieloff, M., Ott, U., Hopp, J., & Schwarz, W. (2021). Solar noble gases in an iron meteorite indicate terrestrial mantle signatures derive from Earth's core. *Nature Comm. Earth Environ*, 2(92), 1–7. https://doi.org/10.1038/s43247-021-00162-2
- Walsh, K., & Levison, H. (2016). Terrestrial planet formation from an annulus. The Astronomical Journal, 152(68). https://doi.org/10.3847/0004-6256/152/3/68
- Wang, K., Lu, X., Liu, X., Zhou, M., & Yin, K. (2022). Partitioning of noble gases (He, Ne, Ar, Kr, Xe) during Earth's core segregation: A possible core reservoir for primordial noble gases. *Geochimica et Cosmochimica Acta*, 321, 329–342. https://doi.org/10.1016/j.gca.2022.01.009
- Willhite, L., Jackson, M., Blichert-Toft, J., Bindeman, I., Kurz, M. D., Halldórsson, S. A., et al. (2019). Hot and heterogenous high-³He/⁴He components: New constraints from proto-Iceland plume lavas from Baffin Island. *Geochemistry, Geophysics, Geosystems*, 20, 5939–5967. https://doi.org/10.1029/2019GC008654
- Williams, C., Mukhopadhyay, S., Rudolph, M., & Romanowicz, B. (2019). Primitive helium is sourced from seismically slow regions in the lowermost mantle. *Geochemistry, Geophysics, Geosystems*, 20, 4130–4145. https://doi.org/10.1029/2019gc008437
- Wu, J., Desch, S. J., Schaefer, L., Elkins-Tanton, L. T., Pahlevan, K., & Buseck, P. R. (2018). Origin of Earth's water: Chondritic inheritance plus nebular ingassing and storage of hydrogen in the core. *Journal of Geophysical Research: Planets*, 123(10), 2691–2712. https://doi. org/10.1029/2018ie005698
- Zhang, Y., & Yin, Q. (2012). Carbon and other light element contents in the Earth's core based on first-principles molecular dynamics. Proceedings of the National Academy of Sciences of the United States of America, 109, 16579–16583. https://doi.org/10.1073/pnas.1203826109

OLSON AND SHARP 18 of 18